DYNAMIC 3D MESH RECONSTRUCTION BASED ON NONRIGID ITERATIVE CLOSEST-FARTHEST POINTS REGISTRATION

Farzam Tajdari, Felix Kwa, Christiaan Versteegh, Toon Huysmans, Yu Song

DYNAMIC 3D MESH RECONSTRUCTION BASED ON NONRIGID ITERATIVE CLOSEST-FARTHEST POINTS REGISTRATION

Farzam Tajdari*
Faculty of
Industrial Design Engineering
Delft University of Technology
f.tajdari@tudelft.nl

Felix Kwa
Faculty of
Industrial Design Engineering
Delft University of Technology
felixkwa@gmail.com

Christiaan Versteegh
R&D Department
BATA Industrials
Best, Netherlands
christiaan.versteegh@bata.com

Toon Huysmans
Faculty of
Industrial Design Engineering
Delft University of Technology
t.huysmans@tudelft.nl

Yu Song
Faculty of
Industrial Design Engineering
Delft University of Technology
y.song@tudelft.nl

ABSTRACT

Fitting apparel and apparel in performing different activities is essential for the functional yet comfortable experience of the user. 4D scans, i.e. 3D scans in continuous timestamps, of the body (part) in performing those activities are the basis for the design of garments/apparel in 4D. In this paper, we proposed a semi-automatic workflow for constructing 4D scans of the body parts with the emphasis on registering noisy scans at a given timestamp. Continuous 3D scans regarding the moving body parts are captured first from different depth cameras from different view angles. In a given timestamp, the collected 3D scans are roughly aligned to a template using the rigid Iterative Closest Points (ICP) algorithm. Then these scans are further registered using a newly proposed non-rigid Iterative Closest-Farthest Points (ICFP) algorithm, in which correspondences between the source and the target are established by either closest or farthest points based on the newly defined logical distance concept and the probability theory. Experimental results indicated that the ICFP method is robust against noise and the scanning accuracy can be as high as 3.4 %. It also reveals that, for the human foot, the differences of ball width and ball angles between the loaded and the unloaded situation can be as large as 8 mm and 2 degrees, respectively. This highlights the importance of using 4D scan in designing garments and apparel.

Keywords: 4D scans, accuracy, robust, non-rigid Iterative Closest-Farthest Points (ICFP), logical distance;

1 INTRODUCTION

Due to comparatively huge changes in shape during deforming a dynamic object, dynamic anthropometry and 4D scanning have attracted a lot of attention in clothing technology recently [1, 2]. The 4D scanning gives valuable information regarding human body deformation during moving, conducting an activity and dynamic workload, establishes the fundamentals of comprehensive ergonomic fit design e.g., personal protective equipment, workwear, sportswear, and other practical garments [3, 4].

The concept of body measurement started with using measurement tape, which was time-consuming and required considerable effort [5]. Advancement in technology introduces the 3D scanning tool-kits [6–11], which improves the effectiveness and

*Address all correspondence to this author.

efficiency of measuring the body shapes [12, 13]. However, the 3D body measuring techniques [14, 15] and scanners only allowed the collecting data in static postures, e.g., hand posture in [16, 17]. Thus, the scan captures the muscular system aiming to hold the static position and neglects the interaction between the body and environment during movement. As a result, garments are still designed based on the anthropometric standard position specified in standards and sizing framework as standing upright, legs hip widespread, arms slightly abducted [18, 19]. However, body proportion diverges from static to dynamic status, especially during intense activities such as sports. Therefore, it is important to investigate the body during motion, to extract meaningful features alterations i.e., dimensions, and transfer the the features into the garment enhancement process. To this end, the technological development from 3D to 4D scanning approaches establishes scanning in motion [20, 21].

Kirk et al. [22] introduced a method to evaluate the raising and lowering of the body surface with respect to connection with position changes via measurement lines on the knee. Schmid et al. [23] proposed seam damages were usually affected by changes of body geometry. The research group of Ashdown studied dimensional variation on the basis of 3D point cloud for the upper and the lower body half [24–26]. Based on the state-of-the-art methodology the deformation of the body surface was studied through discreet static postures. However, there is a paucity of literature regarding measurement alteration during movement and only a few researchers address this challenge [18, 19].

The concept of dynamic anthropometry was prosperously implemented mainly for the enhancement of high-performance sportswear. The challenges were decreasing muscle fatigue, increasing comfort, and resistance diminution and performance development [27, 28]. Firstly, Morlock et al. [29] studied deviation in body measurements from work to sports corresponded postures of men and women that the population sample was very large [19]. Next, body motion is mainly observed through Motion Capture Technology. The method captures the deformation by tracking a few pre-selected landmarks on the body mostly for articulation reconstruction. The approach has broad applications such as video game design, computer-animated movies, or biomechanical analyses in the fields of medicine and sports. The acquisition of 3D surfaces with motion scanning has been studied by many researchers such as [30–33]. A finite number of landmarks highlighted with trackable markers are mounted on the human body and the position of the landmarks was estimated by the systems.

A very recent topic of capturing the dynamic body surface deformation over the moving articulation attracted a lot of attention, as it is often challenged by capture speed, computational speed, and accuracy of the measurements [20]. Most approaches exploit equipment founded on the concept of light and depth sensor technology. Employing techniques and measurement principles i.e., triangulation or light section algorithms, the surfaces are estimated. However, in each time frame, the methods fail to capture the 4D pattern (correspondence) but instead deliver an independant 3D mesh describing shape of the scanned object, which needs higher knowledge to extract the 4D features.

In this paper, we present a workflow of automatically extracting dynamic features from the foot during walking. In detail, the method first aligns 3D point clouds extracted from seven depth cameras around the walking foot through the well-known rigid Iterative Closest Points (ICP) registration method. Then a reference foot model is nonrigidly registered on the aligned 3D raw data to define the patterns and features in each time interval. In the proposed nonrigid ICP algorithm, a new corresponding point selection approach is proposed and implemented for a more effective and effcient registration.

The rest of the paper is presented as follows: first, the methodology is introduced in Section 2 where the techniques of the rigid alignment and nonrigid registration are discussed. In Section 3.1, the setup of the experiments is introduced. In Section 4, experimental results on the comparison of the proposed approach output and the reference data provided by Artec Eva scanner are presented. Finally, a short conclusion is drawn and future research directions are highlighted as well.

2 METHODOLOGY

In this section, we introduce a methodology that reconstructs a temporally corresponded 3D mesh out of different 3D pieces of point cloud through a source mesh, i.e., making a complete 3D shape using a few different depth cameras around the object. For proceeding with the methodology, we use a rigid ICP registration technique to register each piece containing the captured point clouds by each camera, correctly on the source mesh, and then the source mesh will be registered on the combined pieces (target mesh) through a non-rigid ICP registration method. Due to a high degree of noise, the corresponding points selection is modified from only considering the closest point to logical distance selection. The logical distance selection may choose the closest or farthest point on the target to a point on the source as the corresponding point, based on the topology of the reconstructed target. By iteratively reconstructing 3D shape out of the extracted 3D data from each camera in a time frame, we are able to make time series of 3D scans known as 4D scanning.

2.1 Rigid registration

In the proposed research, we focus on the geometry of the foot. Firstly, we estimate the points visible from each camera on the source mesh used in [34] which is scaled to have approximately the same foot length as the scanned data with one of the side cameras (e.g., the red points on a side camera in FIGURE 1 are used to scale the gray source mesh in order to have the same length as the red point-cloud). These estimated points from each

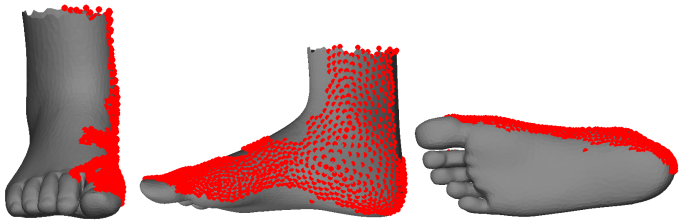

(a) (b) (c)

FIGURE 1: Pre-defined points on the source mesh for a side camera (the camera 3 in FIGURE 3): (a) Front view. (b) Side view. (c) Bottom view.

camera are used as the target for any extracted data from the relevant camera. Then using the rigid ICP method we are able to find the extrinsic transformation matrix that is able to map each piece of data to the correct location on the source mesh. As an example of showing the predefined points on the source mesh, we depicted the predefined points for a side camera in FIGURE 1(e.g., camera 3 described in Section 3.3).

2.2 Filtering

Usually, the output of the depth cameras is very noisy, and also there may be some point clouds that are not presenting any targeted features, e.g. from the background. Thus, first we filter the 3D point cloud of the target mesh ($\mathbb{T}$).In this process, the closest point for each point on $\mathbb{T}$ is found on the source mesh ($\mathbb{S}$), and the distance between each point on $\mathbb{T}$ and its corresponding point on $\mathbb{S}$ are compared with a distance limit (d_l) as follows.

$$d_l = m + 2\sigma \tag{1}$$

where, m is the average of all the closest distance from $\mathbb{T}$ to $\mathbb{S}$, and σ is the standard deviation of the closest distance population. The points that have a distance greater than the d_l will be rejected as follows.

$$\begin{cases} keep, & \text{if } d_p \leq d_l \\ reject, & \text{if } d_p > d_l \end{cases} \tag{2}$$

where d_p is the distance from a point p on $\mathbb{T}$ to its corresponding point on $\mathbb{S}$. It is worth mentioning that we consider the distance from $\mathbb{S}$ to $\mathbb{T}$ only, many useful points on $\mathbb{T}$ might be excluded due to the imperfect alignment of the pieces during establishing the $\mathbb{T}$.

2.3 Nonrigid corresponding selection

In the use of the conventional ICP method, given a point on the $\mathbb{S}$, the closest point on the $\mathbb{T}$ is considered as its corresponding point. As only the Euclidean distance is used in establishing the correspondences, in terms of a high level of noise or disturbances, the topography of the original $\mathbb{S}$ may be lost. Thus, we use a logical distance instead of the closest point approach to establish the correspondences. Accordingly, firstly the closest point from each point on $\mathbb{T}$ to $\mathbb{S}$ is established. Regarding the miss alignment and disturbances for some points, the found distance is comparatively high, which may never be considered as a corresponding point regarding the conventional ICP corresponding point selection algorithm. However, not all the far points are spare as there may be considerable error with rigid registration then some useful points can be located in far distance from the source mesh. In addition if the deformation is very high e.g., closed finger hand as a target versus opened finger hand as a source mesh highlights the disability of using only closest distance to find the correspondences. Thus, we define a varying distance boundary by iteration that increases the probability of finding the useful point although they are far. In the process of finding correspondences from each point on $\mathbb{T}$ to $\mathbb{S}$, each point on $\mathbb{S}$ may be selected for more than one point on the $\mathbb{T}$. In this case, we logically select either the closest or farthest point. In each iteration of the registration process, we define a boundary distance as follows for the corresponding distance matrix from $\mathbb{T}$ to $\mathbb{S}$ as follows.

$$Bound = m + \zeta\sigma \tag{3}$$

where m and σ are the mean and standard deviation of the counted distance for the correspondences from $\mathbb{T}$ to $\mathbb{S}$, accordingly. If for a point on $\mathbb{S}$ a population of points $\mathbb{T}$ are selected which includes more than one point, then we consider the point with the highest distance among the population, if all the distance for the population is greater than the bound. Otherwise, we select the closest point as the corresponding point to the point on $\mathbb{S}$. The process of the corresponding point selection is explained in Algorithm 1.

Discussion: To study the probability of success with the considered value in (3), statistical solutions are employed. First, we assume that the closest distance from points on $\mathbb{T}$ to points on $\mathbb{S}$ establishes a normally distributed population with an average of m and standard deviation of σ. Accordingly and based on Miller's studies of Freund's statistics [35] used in [36–38], the probability indicator z is defined as follows.

$$z = \frac{Bound - m}{\sigma} \tag{4}$$

$$= \frac{m + \zeta\sigma - m}{\sigma} = \zeta \tag{5}$$

Using Table III of the book [35], while $z = \zeta$, the probability (P)

Algorithm 1 The proposed corresponding selection approach

Input: Target point clouds ($\mathbb{T}$) and Source point clouds ($\mathbb{S}$)
Output: Corresponding points

Initialization
SourceID: Find the closest point from each point on $\mathbb{T}$ to a point on $\mathbb{S}$
SourceDis: The distance between the two corresponding points regarding SourceID
IDclass = unique(SourceID): Defines all the involved points from source as correspondences
Bound = mean(SourceDis) + std(SourceDis)
$k = 1$
while $k \leq$ length(IDclass) **do**
  ResembleID = find(SourceID == IDclass(k))
  DistanceMatrix = SourceDis(SourceID(ResembleID))
  if isempty(find(SourceDis(ResembleID)<Bound,1)) **then**
    The corresponding point is the farthest
  else
    The corresponding point is the closest
  end if
  $k = k+1$
end while

of having a distance more than the bound is

$$P(Distance > Bound) = 0.5 - P(z) = 0.5 - P(\zeta) \qquad (6)$$

It should be noted that in the Table III of the book, z is bounded where $z \in [0,\ 3.09]$ which $0 \leq P(z) \leq 0.499$. Thus, $P(Distance > Bound)$ is always equal or less then 0.5. As the methodology is iterative with a maximum iteration of $j^{\max}$, the probability of missing a useful point would be $P(Distance > Bound)^{j^{\max}}$ which would be a very small value. In fact, greater values of the *Bound* resulted from greater values of ζ, means the closest point which is often used in the conventional ICP algorithm is addressed in the selection. While, smaller values of the *Bound* (smaller value of ζ) emphasises more on selecting the farthest point which may map all the source mesh vertices to the farthest point and results in the source mesh topology loss. There must be an optimal value of ζ that balances the closest and farthest selection process as discussed in Section 3.2.

2.4 Nonrigid registration

In this section, based on the established correspondences, a cost function based on Amberg [39] is defined. Amberg [39] proposed the non-rigid registration formulation as a combination of distance and stiffness terms summarised in the following formula

$$\begin{aligned} E(X) &= \| \begin{bmatrix} \alpha M \otimes G \\ WD \end{bmatrix} X - \begin{bmatrix} 0 \\ WU \end{bmatrix} \|_F^2 \\ &= \|AX - B\|_F^2 \end{aligned} \qquad (7)$$

where, The sparse matrix D is formed to facilitate the transformation of the source vertices with the individual transformations contained in X via matrix multiplication, and denoted as $D = diag(v_1^T, v_2^T, \ldots, v_n^T)$, where $v_i \in \mathbb{S}$ and $i = 1, ..., n$, and n is the number of vertices on the $\mathbb{S}$. W is a diagonal matrix consisting of weights w_i. α is the stiffness constraint. To regularise the deformation, an additional stiffness term is introduced. Using the Frobenius norm $\|.\|_F$, the stiffness term penalizes the difference of the transformations of neighboring vertices, through a weighting matrix $G = diag(1, 1, 1, \gamma)$. During the deformation, γ is a parameter to stress differences in the skew and rotational part against the translational part of the deformation. The value of γ can be specified based on data units and the types of deformation [39]. The node-arc incidence matrix M (e.g. Dekker [40]) of the template mesh topology is employed to convert the stiffness term functional into a matrix form. As the matrix is fixed for directed graphs, the construction is one row for each edge of the mesh and one column per vertex. To establish the node-arc incidence matrix of the source topology, the indices (i.e. the subscripts) of edges and vertices are addressed, for any edge of r which is connected to vertices (i, j) , in r^{th} row of M, and the nonzero entries are $M_{ri} = -1$ and $M_{rj} = 1$.

3 EXPERIMENT SETUP

3.1 Parameters of the proposed method

Table 1 presents parameters used in the experiment. During the minimization of the cost function, γ in G introduced in (7), was chosen to one. The stiffness constraint, α, is the lowering scalar. In the experiments α is decreasing from 1000 to 1. Regarding dependency of α values to the dynamic of source surface, the bounds of these values were manually defined so that only global deformations were considered in the beginning of registration. On the other hand, the lower limit of the α also depend on the data type [39]. Accordingly, a small α may cause singularity of A in Eq. (7), which leads to instability of the solution. Therefore, our experiments started with a sufficiently high α.

To have a smoother registration process, we averaged a number of points from a set with size of 3 (N_{mean} = 3). In the implementation of [41], the system of linear equations that arises in each step was solved with the help of the UMFPACK library [42].

TABLE 1: Parameters used in simulation configuration.

Parameter	Value	Description
α	1000:1	stiffness ratio
N_{mean}	3	Target points averaging size
ε	0.001	Convergence error threshold
$j^{\max}$	50	Convergence iteration threshold
$k^{\max}$	20	Number of iteration for the outer loop

TABLE 2: Components of the final product in FIGURE 3.

Part Number	Description	Application
0-6	RealSense D435i	capturing 3D point cloud
7-8	AdaFruit VL53L0X ToF stance sensors	Define start and end of scanning

3.2 Tuning of ζ

In this section we numerically investigate the percentage of mean mesh quality loss and percentage of the target vertices involved in the nonrigid registration for a domain of ζ. There is an optimum point which maximise the involved vertices and minimises the mesh quality loss. Accordingly, we consider a cost function as follows.

$$\min J = \sum \frac{|\bar{Q}^{final} - \bar{Q}^{0}|}{\bar{Q}^{0}} + \frac{N_{in}^{T}}{N_{tot}^{T}} \tag{8}$$

where $\bar{Q}^{final}$ and $\bar{Q}^{0}$ are the average of mesh quality for all vertices on the source mesh before and after registration respectively. Also, N_{in}^{T} is the number of vertices from target employed as corresponding points during the nonrigid registration process, and N_{tot}^{T} is the total number of vertices on the target mesh. As stated in Section 2.3, ζ equals to z and has an acceptable range in $[0,\ 3.09]$. The results reported in FIGURE 2 shows best performance where $\zeta = 1.7$.

3.3 Scanner introduction

The scanner used in this study is the first prototype of a 4D foot scanner at TUDelft [43]. As shown in FIGURE 3 and reported in TABLE 2, the scanner utilizes seven RealSense D435i depth cameras to capture a 4D foot scan.

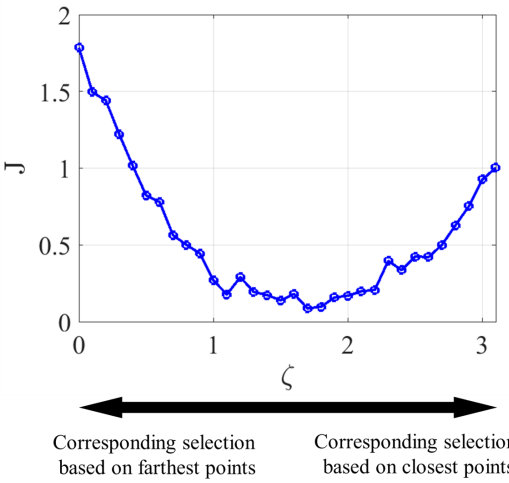

FIGURE 2: Variation of J for a domain of ζ.

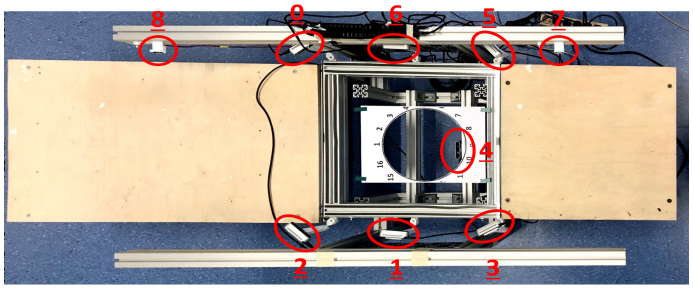

FIGURE 3: Scanner.

4 RESULTS

4.1 Raw data

Using the scanner, we were able to capture the geometric shape of the foot as shown in FIGURE 4(a), which is very noisy and the foot part is not the majority of the extracted data. Thus, we manually deleted the spare parts through MeshLab software. In which the result is depicted in FIGURE 4(b).

4.2 Frame selection

During scanning a foot many frames are captured by each camera while the captured frames are not synchronised with each other. In this paper, we manually looked at the frame by frame extracted with each camera and picked the ones that corresponded to the same posture. We considered five main postures as shown in FIGURE 5 as: 1. Heel strike, 2. Foot-flat, 3. Mid-stance, 4. Heel-off, and 5. Toe-off. Accordingly, the selected frames from an experiment is shown in FIGURE 6.

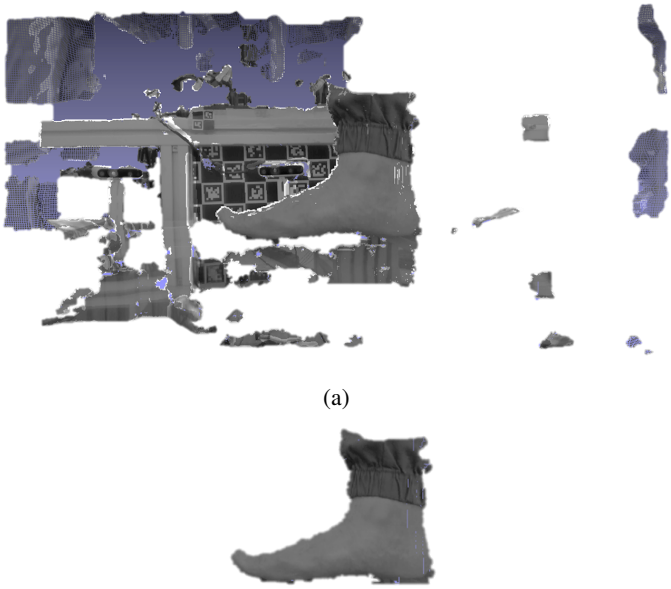

(a) (b)

FIGURE 4: Raw data from one of the RealSense depth camera: (a) Uncleaned. (b) Cleaned.

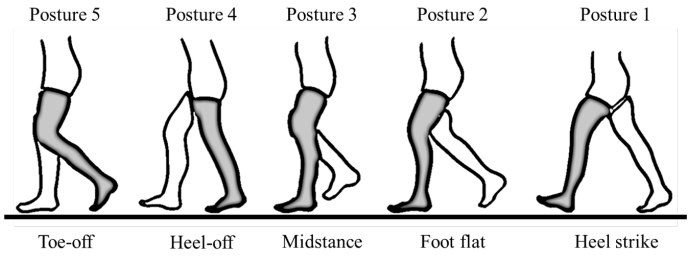

FIGURE 5: Main postures during walking.

4.3 Accuracy

Employing the discussed technique in Section 2, we assess the accuracy of the scanner through two static 3D objects of human foot and human hand as follows.

4.3.1 Foot model: The used source mesh is shown in FIGURE 7(a). To evaluate the effectiveness of the introduced algorithm, we scanned a foot with an Artec Eva scanner in a no-load case as shown in FIGURE 7(b), then the scanned foot was printed out via Ulimaker S5 scanner shown in FIGURE 7(c). The printed foot is scanned with our scanner in static mode which is compared with the scan data of using the Artec Eva. Next, some dimensions shown in FIGURE 8 are compared between the two scanners' output. We firstly find the scaling ratio which maps the

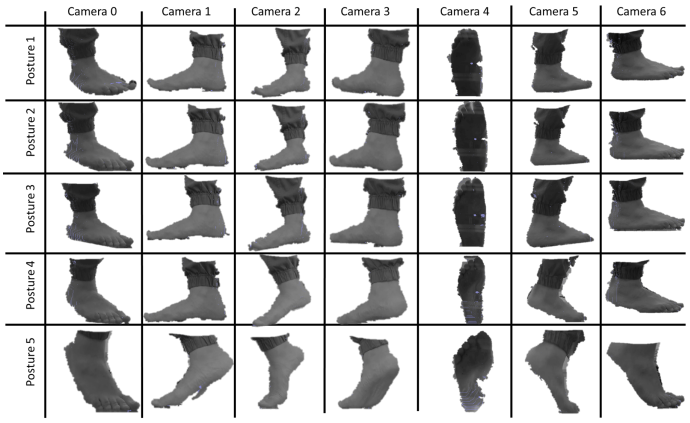

FIGURE 6: Selected frames.

(a) (b) (c)

FIGURE 7: No-load foot. (a) The source mesh. (b) Scanned through Artec Eva scanner. (c) Printed Artec Eva output via Ultimaker S5 printer.

length of the reconstructed foot to the length of the foot collected with the Artec Eva scanner and then calculate the errors for the other dimensions as width, ball width, and ball angle according to [44]. Based on FIGURE 8, L_r, W_r, BW_r, and α_r explain the length, width, ball width, and ball angle of the scanned foot with the Artec Eva scanner respectively. And, L_e, W_e, BW_e, and α_e define the length and width of the estimated foot through our method respectively. The scaling factor of r is considered as follows,

$$r = \frac{L_r}{L_e} \tag{9}$$

where in our experiment, $L_r = 222.2$ mm, $L_e = 0.3561$ mm which results in $r = 623.9$. Thus any dimension extracted from our method is multiplied to the r and compared with the corresponded values on the Artec Eva scanner output summarised in TABLE 3. According to the table, the errors for the width is 3.2 mm, for the ball width is 3.4 mm, and for the ball angle is 0.9°, which shows the average percentage error is about 3.4%.

4.3.2 Hand model: As an extra validation, we used a hand model in [6] as shown in FIGURE 9. According to the

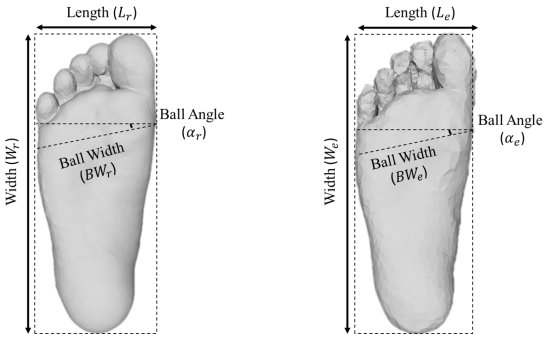

(a) (b)

FIGURE 8: Dimension definition: (a) Artec Eva. (b) Our method.

TABLE 3: Error results of the parameters introduced in FIGURE 8 while the scaling ratio $r = 623.9$.

Parameter	Artec Eva	Our approach	MAE
Width (mm)	$W_r = 87.3$	$r \times W_e = 84.1$	3.2
Ball Width (mm)	$BW_r = 92.6$	$r \times BW_e = 89.2$	3.4
Ball Angle	$\alpha_r = 10.8°$	$\alpha_e = 11.7°$	0.9°

figure, the 3D printed hand, the Artec Eva scan of the hand, the used source mesh, and the output of our scanner are depicted in FIGURE 9(a), (b), (c), and (d) respectively. Furthermore, we rigidly aligned the output of our scanner with the Artec Eva scan as shown in FIGURE 9(e) to visually compare the accuracy of the output. To numerically investigate the deviation of our scanner output with the Artec eva scan we figured the histogram of the distance between a point on our scan and its closest point on the Artec eva scan. Accordingly, the average error is about 2 mm which is acceptable in ergonomics study.

4.4 Posture reconstruction

Through the explained method in this paper, we use seven cleaned frames for each posture as the input of the proposed method. Accordingly, the output is depicted in FIGURE 11 for the bottom view and the side view of the reconstructed scans of one foot shown in FIGURE 6 over three feet we reconstructed in this paper. The deformation of the source mesh is logically related to the corresponded posture, which shows the acceptable visual performance of the approach. In addition, the deformation of each the foot width is compareable between adjacent frames, where the posture with more load on front of foot has bigger width shown in FIGURE 11. To study the deformation numerically, we reported the introduced dimensions in Section "Accuracy", for different postures per case in FIGURE 12 which shows the deformation direction of all the feet are the same however the amplitude is different. The feet belong to three cases as follows:

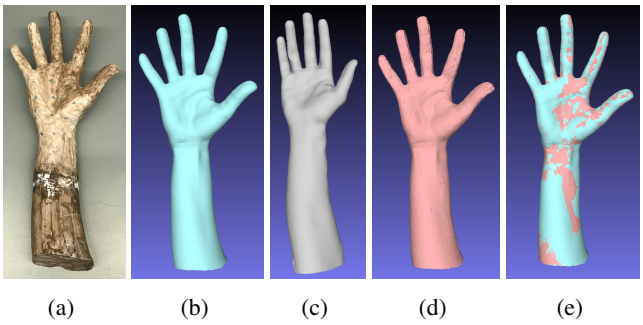

(a) (b) (c) (d) (e)

FIGURE 9: Hand evaluation: (a) Real model. (b) Artec Eva scan. (c) Source mesh. (d) Our method scan. (e) Aligned our output to Artec Eva scan.

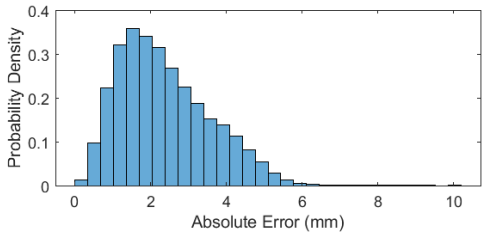

FIGURE 10: Error sparsity histogram.

Case 1: Male, from Middle-east, 30 years old, with Body Mass Index (BMI) equal to 27.8.
Case 2: Male, from Asia, 25 years old, with BMI equal to 26.8.
Case 3: Male, from Europe, 24 years old, with BMI equal to 21.9.

The figure shows the variation of the foot per case in different postures and please note that in the posture 5, the length of the foot is not the real length and is the distance between tip of the big toe to the heel of the foot, and the bending of the foot is not considered. This resulted in a sudden decrease of the foot length in the figure.

5 CONCLUSION

The method presented in this paper demonstrates a workflow of extracting any time-varying features from dynamic scans of a deformable object. The semi-automated procedure includes predefining points which may be seen by each depth camera, manually cleaning the raw data from each camera, rigid registration

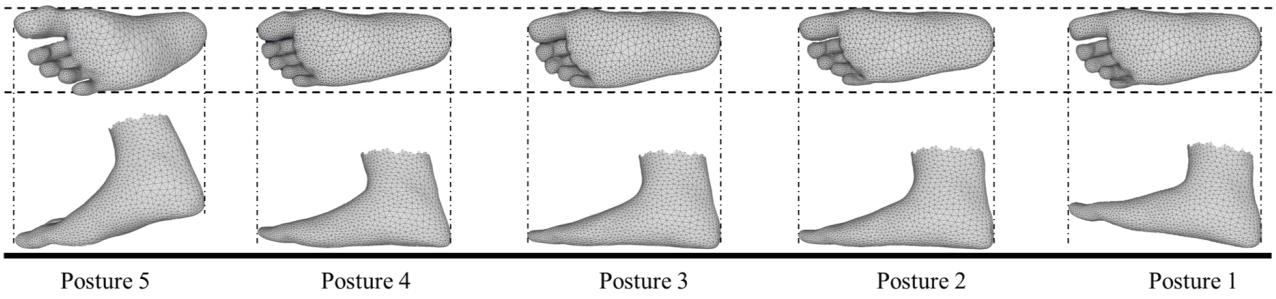

FIGURE 11: Results of posture reconstruction for the case 1.

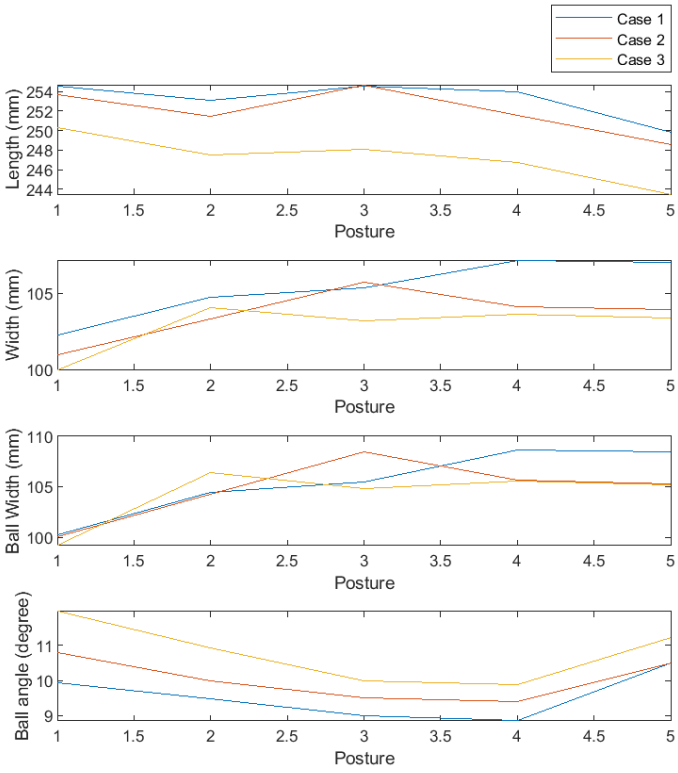

FIGURE 12: Results per different cases.

of the extracted data from each camera to the corresponded predefined points, and finally non-rigidly registering a source mesh on the point cloud reconstructed through the rigid registration. Reconstructing the final mesh through the non-rigid registration for several frames in a time series provides a 4D feature outcome (for specific points) or 4D trackable scanning (for all the points) which is unique. Comparison of the output of our algorithm with the dimensions extracted from the scanning data of the same object using an Artec Eva scanner shows the estimated dimensions have acceptable error. Further developments include deriving a full automated approach for the filtering, the predefined point selection, and corresponded frame selection, a higher frequency scanner, and integrating temporal super-resolution repetitive motion techniques to have higher resolution of the 4D scanning.

ACKNOWLEDGMENT

This work is supported by Dutch NWO Next UPPS - Integrated design methodology for Ultra Personalised Products and Services project under Grant 15470.

REFERENCES

[1] Boorady, L. M., Rucker, M., Haise, C., and Ashdown, S. P., 2009. "Protective clothing for pesticide applicators: A multimethod needs assessment". *Journal of Textile and Apparel, Technology and Management,* ***6***(2).

[2] Bye, E., Labat, K. L., and Delong, M. R., 2006. "Analysis of body measurement systems for apparel". *Clothing and Textiles Research Journal,* ***24***(2), pp. 66–79.

[3] Boorady, L. M., 2011. "Functional clothing—Principles of fit".

[4] Minnoye, A., Tajdari, F., Doubrovski, E., Wu, J., Kwa, F., Elkhuizen, W., Huysmans, T., and Song, Y., 2022. "PERSONALIZED PRODUCT DESIGN THROUGH DIGITAL FABRICATION". *International Design Engineering Technical Conferences & Computers and Information in Engineering Conference*.

[5] Schmid, U., and Mecheels, J., 1981. "Kräfte an Textilien und Nähten der Kleidung in Abhängigkeit von Körperbewegungen und Kleidungsschnitt'". *Bekleidung und Wäsche,* ***33***, pp. 77–82.

[6] Yang, Y., Xu, J., Elkhuizen, W. S., and Song, Y., 2021. "The development of a low-cost photogrammetry-based 3D hand scanner". *HardwareX,* ***10***, p. e00212.

[7] Elkhuizen, W., Essers, T., Song, Y., Geraedts, J., Weijkamp, C., Dik, J., and Pont, S., 2019. "Gloss, color, and topography scanning for reproducing a Painting's appearance using 3D printing". *Journal on Computing and Cultural Heritage (JOCCH),* ***12***(4), pp. 1–22.

[8] Tajdari, F., Toulkani, N. E., and Zhilakzadeh, N., 2020. "Semi-real evaluation, and adaptive control of a 6dof surgical robot". In 2020 11th Power Electronics, Drive Systems, and Technologies Conference (PEDSTC), IEEE, pp. 1–6.

[9] Tajdari, F., Toulkani, N. E., and Zhilakzadeh, N., 2020. "Intelligent optimal feed-back torque control of a 6dof surgical rotary robot". In 2020 11th Power Electronics, Drive Systems, and Technologies Conference (PEDSTC), IEEE, pp. 1–6.

[10] Tajdari, F., Tajdari, M., and Rezaei, A., 2021. "Discrete time delay feedback control of stewart platform with intelligent optimizer weight tuner". In 2021 IEEE International Conference on Robotics and Automation (ICRA), IEEE, pp. 12701–12707.

[11] Tajdari, F., and Ebrahimi Toulkani, N., 2021. "Implementation and intelligent gain tuning feedback–based optimal torque control of a rotary parallel robot". *Journal of Vibration and Control*, p. 10775463211019177.

[12] Choi, S., and Ashdown, S. P., 2011. "3D body scan analysis of dimensional change in lower body measurements for active body positions". *Textile research journal,* ***81***(1), pp. 81–93.

[13] Tajdari, F., Eijck, C., Kwa, F., Versteegh, C., Huysmans, T., and Song, Y., 2022. "Optimal Position of Cameras Design in a 4D Foot Scanner". *International Design Engineering Technical Conferences & Computers and Information in Engineering Conference*.

[14] Goto, L., Lee, W., Molenbroek, J. F. M., and Goossens, R., 2015. "Analysis of a 3D anthropometric data set of children for design applications". In Proceedings 19th Triennial Congress of the IEA, Vol. 9, p. 14.

[15] Tajdari, M., Pawar, A., Li, H., Tajdari, F., Maqsood, A., Cleary, E., Saha, S., Zhang, Y. J., Sarwark, J. F., and Liu, W. K., 2021. "Image-based modelling for adolescent idiopathic scoliosis: mechanistic machine learning analysis and prediction". *Computer methods in applied mechanics and engineering,* ***374***, p. 113590.

[16] Yang, Y., Yuan, T., Huysmans, T., Elkhuizen, W. S., Tajdari, F., and Song, Y., 2021. "Posture-invariant three dimensional human hand statistical shape model". *Journal of Computing and Information Science in Engineering,* ***21***(3).

[17] Yang, Y., Zhou, H., Song, Y., and Vink, P., 2021. "Identify dominant dimensions of 3D hand shapes using statistical shape model and deep neural network". *Applied Ergonomics,* ***96***, p. 103462.

[18] Ashdown, S. P., 2011. "Improving body movement comfort in apparel". In *Improving comfort in clothing*. Elsevier, pp. 278–302.

[19] Morlock, S., Lörcher, C., and Schenk, A., 2016. "Entwicklung eines ergonomisch-und bewegungsorientierten Größensystems für Funktionsmaße zur optimierten Gestaltung von Berufs-und Schutzbekleidung". *IGF Project,* ***18993***.

[20] Temporal-3dMD Systems (4D). Available:, 10.

[21] 4D Dynamic Scanner. Available:, 10.

[22] Kirk Jr, W., and Ibrahim, S. M., 1966. "Fundamental relationship of fabric extensibility to anthropometric requirements and garment performance". *Textile Research Journal,* ***36***(1), pp. 37–47.

[23] Schmid-Schönbein, G. W., Sung, K. L., Tözeren, H., Skalak, R., and Chien, S., 1981. "Passive mechanical properties of human leukocytes". *Biophysical Journal,* ***36***(1), pp. 243–256.

[24] Choi, S.-Y., and Ashdown, S. P., 2010. "Application of lower body girth change analysis using 3D body scanning to pants patterns". *Journal of the Korean Society of Clothing and Textiles,* ***34***(6), pp. 955–968.

[25] Lee, J., and Ashdoon, S. P., 2005. "Upper body surface change analysis using 3-D body scanner". *Journal of the Korean society of clothing and textiles,* ***29***(12), pp. 1595–1607.

[26] Choi, J., and Hong, K., 2015. "3D skin length deformation of lower body during knee joint flexion for the practical application of functional sportswear". *Applied Ergonomics,* ***48***, pp. 186–201.

[27] Zakaria, N., 2014. "Infants and children: Understanding sizing, body shapes and apparel requirements for infants and children". In *Designing Apparel for Consumers*. Elsevier, pp. 95–131.

[28] Klepser, A., and Morlock, S., 2020. "4D Scanning-Dynamic View on Body Measurements". *Communications in Development and Assembling of Textile Products,* ***1***(1), pp. 30–38.

[29] Loercher, C., Morlock, S., and Schenk, A., 2018. "Design of a motion-oriented size system for optimizing professional clothing and personal protective equipment". *Journal of Fashion Technology*.

[30] Park, S. I., and Hodgins, J. K., 2006. "Capturing and animating skin deformation in human motion". *ACM Transactions on Graphics (TOG),* ***25***(3), pp. 881–889.

[31] Aguiar, E., 2014. "Performance Capture Methods". In Proceedings of the European Conference on Computer Vision (ECCV), Zürich, Swiss.

[32] Wu, C., Varanasi, K., Liu, Y., Seidel, H.-P., and Theobalt, C., 2011. "Shading-based dynamic shape refinement from multi-view video under general illumination". In 2011 International Conference on Computer Vision, IEEE, pp. 1108–1115.

[33] Fit to Deformation. Available:, 10.

[34] Tajdari, F., Huysmans, T., Yang, Y., and Song, Y., 2022. "Feature preserving non-rigid iterative weighted closest point and semi-curvature registration". *IEEE Transactions on Image Processing*, p. 1.

[35] Freund, J. E., Miller, I., and Miller, M., 2004. *John E. Fre-*

und's Mathematical Statistics: With Applications. Pearson Education India.

[36] Tajdari, F., Ghaffari, A., Khodayari, A., Kamali, A., Zhilakzadeh, N., and Ebrahimi, N., 2019. "Fuzzy control of anticipation and evaluation behaviour in real traffic flow". In 2019 7th International Conference on Robotics and Mechatronics (ICRoM), IEEE, pp. 248–253.

[37] Tajdari, F., Toulkani, N. E., and Nourimand, M., 2020. "Intelligent architecture for car-following behaviour observing lane-changer: Modeling and control". In 2020 10th International Conference on Computer and Knowledge Engineering (ICCKE), IEEE, pp. 579–584.

[38] Tajdari, F., Golgouneh, A., Ghaffari, A., Khodayari, A., Kamali, A., and Hosseinkhani, N., 2021. "Simultaneous intelligent anticipation and control of follower vehicle observing exiting lane changer". *IEEE Transactions on Vehicular Technology,* ***70***(9), pp. 8567–8577.

[39] Amberg, B., Romdhani, S., and Vetter, T., 2007. "Optimal step nonrigid icp algorithms for surface registration". In 2007 IEEE Conference on Computer Vision and Pattern Recognition, IEEE, pp. 1–8.

[40] Dekker, M., 1986. "Mathematical programming". *CRC, May,* ***4***.

[41] Charlie, N., 2020. *nricp - Non-rigid iterative closest point*.

[42] Davis, T. A., 2004. "Algorithm 832: UMFPACK V4. 3—an unsymmetric-pattern multifrontal method". *ACM Transactions on Mathematical Software (TOMS),* ***30***(2), pp. 196–199.

[43] Kwa, F. S. S., 2021. "Design of an accurate and low cost 4D foot scanner for podiatrists".

[44] Tang, U. H., Siegenthaler, J., Hagberg, K., Karlsson, J., and Tranberg, R., 2017. "Foot anthropometrics in individuals with diabetes compared with the general Swedish population: Implications for shoe design". *Foot Ankle Online J,* ***10***(3), p. 1.